Magnetic susceptibility and phase transitions in $LiNiPO_4$

S. Lewińska,[1] A. Szewczyk,[1,*] M. U. Gutowska,[1] J. Wieckowski,[1] R. Puzniak,[1] R. Diduszko,[1] A. Reszka,[1] B. J. Kowalski,[1] Yu. Kharchenko,[2] and J. Molenda[3]

[1]*Institute of Physics, Polish Academy of Sciences, Aleja Lotnikow 32/46, 02-668 Warsaw, Poland*

[2]*B. Verkin Institute for Low Temperature Physics and Engineering of the NASU, 47 Nauky Ave., Kharkiv, Ukraine*

[3]*Faculty of Energy and Fuels, AGH University of Science and Technology, Mickiewicza 30, 30-059 Krakow, Poland*

(Received 25 January 2019; revised manuscript received 10 June 2019; published 27 June 2019)

Detailed studies of specific heat, magnetization, and magnetic torque of a single crystal of $LiNiPO_4$ olivine are presented. Olivines attract attention as promising for application as cathodes in Li-ion batteries and exhibiting a unique set of properties. $LiNiPO_4$ is the unique olivine, in which antiferromagnetic order develops in two steps, i.e., at 21.8 K, the second-order transition to an incommensurate phase and then, at 20.9 K, the first-order transition to a commensurate phase appears. Specific heat studies, supplemented by the "slope analysis procedure," revealed a splitting of the specific heat anomaly accompanying the first-order transition, which suggests that actually, these are two coupled transitions, one of which can be the ferroelectric one. The specific heat was measured as a function of temperature for a series of fixed external magnetic field B values. As the result, analytical equations describing the phase transition lines in the T-B plane were determined and evolution of a shape of the specific heat anomalies accompanying the phase transitions, observed in the powder sample under influence of B, was modeled. Angular dependence of magnetic torque and of magnetization for B rotating within the a-c and b-c crystalline planes was measured for several fixed temperature and B values. Based on these results, we found a new effect, that we called "off-diagonal nonlinear magnetic susceptibility," i.e., we found that for each main crystallographic axis (a, b, and c), an additional component of magnetic susceptibility, proportional to the square of the perpendicular to this axis component of B, exists. A phenomenological model of this effect, describing the experimental results correctly, was proposed.

DOI: 10.1103/PhysRevB.99.214440

I. INTRODUCTION

Magnetic LiTPO$_4$ olivines, where T stands for Mn, Fe, Co, or Ni, attract considerable attention as materials for cathodes of Li-ion batteries [1–8] and as compounds exhibiting a unique set of physical properties not elucidated satisfactorily yet. They show an exceptionally large linear magnetoelectric effect, however, the issue of existence of a ferroelectric order in them is not clarified yet.

The olivines crystallize in the orthorhombic *Pnma* structure (space group No. 62), Fig. 1. The unit cell contains four magnetic T ions, forming four magnetic sublattices. Several ways of numbering them are used and we apply the convention of numbering and describing the exchange constants used in Refs. [9,10]. According to it, the T^{2+} ions occupy the 4c positions: 1 $(x, \frac{1}{4}, z)$, 2 $(x+\frac{1}{2}, \frac{1}{4}, -z+\frac{1}{2})$, 3 $(-x, \frac{3}{4}, -z)$, 4 $(-x+\frac{1}{2}, \frac{3}{4}, z+\frac{1}{2})$. For $LiNiPO_4$, $x \approx 0.28$, $z \approx 0.98$, and the lattice constants are equal to $a = 10.02$ Å, $b = 5.83$ Å, and $c = 4.66$ Å.

In the olivine structure, "corrugated" (100) oriented T–O layers can be distinguished. Within them, magnetic moments of the neighboring T^{2+} ions, each of which is surrounded by six O^{2-} ions forming a corner sharing octahedron, Fig. 1, are strongly coupled antiferromagnetically by T–O–T superexchange interactions. In turn, the T^{2+} ions located within neighboring (100) layers are coupled weakly by higher order, e.g., T–O–P–O–T, superexchange interactions [9–12]. The T^{2+} magnetic moments show very large uniaxial magnetic anisotropy with the easy axis different for different T ions. Due to the facts enumerated above, the magnetic olivines behave usually as quasi-two-dimensional Ising systems that order antiferromagnetically at the Néel temperature, ranging from ≈21 K for $LiNiPO_4$ to ≈50 K for $LiFePO_4$.

Generally, the magnetic olivines containing various T ions exhibit similar physical properties, however, two of them, $LiCoPO_4$ and $LiNiPO_4$, deserve particular attention. As it was shown by neutron scattering [11], magnetization [11,13,14], magnetic torque [15], and specific heat [15] studies, $LiCoPO_4$ has a small nonzero spontaneous magnetization and its magnetic structure has not higher than monoclinic symmetry, e.g., the $P12_1'1$ symmetry, consistent with the presence of an intriguing ordering of toroidal moments [11]. It should be mentioned that the observation of the ferrotoroidic domains [16] is controversial and was questioned [15,17]. Moreover, $LiCoPO_4$ shows an original additional magnetic phase transition below the Néel temperature, related to a change in the anisotropy of the system [15].

$LiNiPO_4$, in turn, is a unique olivine, in which the antiferromagnetic order develops in two steps. On lowering temperature, at first, the second-order transition to the modulated, incommensurate antiferromagnetic phase, IC, appears at $T_{N1} =$ 21.8 K and then, the first-order transition to the commensurate antiferromagnetic phase, C, appears at $T_N = 20.9$ K.

*szewc@ifpan.edu.pl

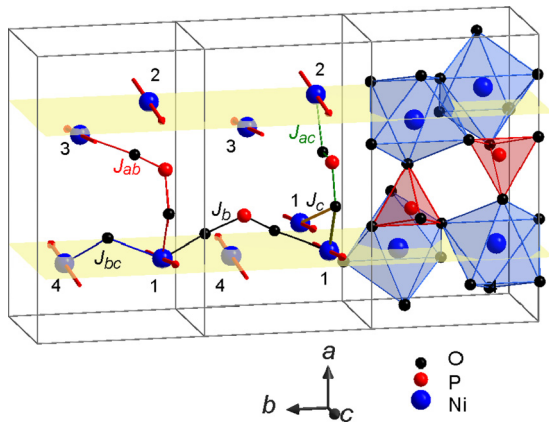

FIG. 1. $LiNiPO_4$ structure in a commensurate phase. Three unit cells with hidden Li and some O ions are shown. Oxygen polyhedra surrounding Ni and P are shown in one cell. In two others, Ni^{2+} magnetic moments and some superexchange interaction paths, denoted with the symbols of exchange integrals to which they contribute, are drawn.

Based on the neutron [9,18–21], magnetization [9,19,22,23], magnetooptical [24], and electric polarization [19,22] studies, the phase diagram of $LiNiPO_4$ in the temperature (T) - magnetic field (B) coordinates, for B up to 30 T, was constructed [19,20,22]. Moreover, there were determined, Table I: (i) D_a and D_b constants characterizing the single-ion anisotropy energy along the a and b axis, respectively, at $D_c = 0$, (ii) J_{bc} exchange integral characterizing the superexchange interactions between the 1-4 and 2-3 Ni^{2+} ions, being the nearest neighbors, NN, within the corrugated (100) planes, (iii) J_b and J_c integrals of the superexchange interactions between the i-i (i = 1, 2, 3, and 4) Ni^{2+} ions, being the next nearest neighbors, NNN, within the corrugated (100) planes, along the b and c axis, respectively, (iv) integrals of the superexchange interactions between the Ni^{2+} ions located within neighboring (100) planes, i.e., the 1-3 and 4-2 interaction integral J_{ab} and the 1-2 and 4-3 interaction integral J_{ac}, and (v) the Dzyaloshinsky vector of length D_{14}, parallel to the b axis, describing the Dzyaloshinsky-Moriya, D-M, anisotropic 1-4 and 3-2 exchange interactions. In Table I, the positive (negative) exchange constants denote the antiferromagnetic (ferromagnetic) coupling. The ± sign at the D_{14} parameter of the D-M interactions denotes that the sign of canting of the particular sublattices was not determined by the neutron studies.

As the result of the complex interactions enumerated above, in $LiNiPO_4$, the c axis is the preferred direction of orientation for spins of all the sublattices, and the b axis is the hardest one. In the low-temperature antiferromagnetic phase, magnetic moments of the 1 and 2 (as well as 3 and 4) ions located within neighboring (100) planes and within the same (010) plane are ordered nearly ferromagnetically, mainly due to the negative J_{ac} value. Simultaneously, the magnetic moments of the ions located within the same corrugated (100) planes, i.e., of the 1 and 4, as well as 2 and 3 ions, are ordered nearly antiferromagnetically. Origins of the ordering appearing within the (100) planes are more complex. Though the NN (1-4 and 2-3) interactions, characterized by the $J_{bc} > 0$ constant, and the weaker interplanar (1-3 and 4-2) interactions, characterized by the $J_{ab} > 0$ constant, support the observed antiferromagnetic order, the NNN i-i (i = 1, 2, 3, and 4) interactions, characterized by the $J_b > 0$ constant, are antiferromagnetic too, which means that the observed antiferromagnetic order appears as the result of frustration of the NN and NNN interactions. Thus, a commensurate antiferromagnetic structure of the C_z type, i.e., the structure in which parallel to the c axis component of the vector $\mathbf{C} = \mathbf{S}_1 + \mathbf{S}_2 - \mathbf{S}_3 - \mathbf{S}_4$ is nonzero, is the ground state structure at low temperatures. However, the tendency for forming incommensurate, modulated structures appears in high magnetic field $B > 12$ T, as well as within a narrow temperature range of ∼1 K near the Néel temperature, even in small B. This is illustrated in the phase diagram published in Ref. [20]. Additionally, presence of the D-M interactions leads to a small canting of the magnetic moments of particular sublattices and as the result, a small nonzero component of the $\mathbf{A} = \mathbf{S}_1 - \mathbf{S}_2 - \mathbf{S}_3 + \mathbf{S}_4$ vector along the a axis appears.

TABLE I. Exchange and anisotropy constants determined for $LiNiPO_4$ in Refs. [10,20], given in meV.

J_{bc}	J_b	J_c	J_{ab}	J_{ac}	D_a	D_b	D_{14}
1.04	0.670	−0.05	0.30	−0.11	0.339	1.82	±0.32

The low-temperature commensurate magnetic structure, denoted as C, breaks the inversion symmetry, but it is invariant with respect to the twofold screw axis along b. Thus it is inconsistent with the presence of any spontaneous electric polarization [9]. However, the magnetic field applied along the c axis disturbs canting of the different sublattices, breaks the twofold symmetry and induces electric polarization along the a axis. A similar effect appears in the magnetic field applied along the a axis. Then, the electric polarization is induced along the c axis. These considerations obey, if the material shows no spontaneous magnetization, because nonzero magnetization breaks the symmetry in the same way as the magnetic field does. For many years, it was assumed that $LiNiPO_4$ shows an ideal antiferromagnetic ordering, however the presence of a very small nonzero spontaneous magnetization of ∼4.5 A/m below 5 K, parallel to the c axis, was reported in Ref. [23]. Thus the existence of a spontaneous polarization within the low-temperature commensurate phase can not be ruled out *a priori*.

On the contrary, the incommensurate structure [9,20], which appears about 1 K above T_N and has a form of a linearly polarized structure modulated along the b axis with the modulation vector [0, q, 0] decreasing on lowering temperature from $q = 0.155$ at T_{N1} to $q = 0.07$ at T_N, preserves the inversion symmetry and thus, can not be accompanied by a spontaneous electric polarization.

II. AIMS, METHODS, AND SAMPLES

In view of the above facts, we focused on verifying, if any signatures of existence of a phase transition to the ferroelectric phase appear in $LiNiPO_4$, and on studying, if the complex interactions and magnetic structures existing in $LiNiPO_4$

result in any uncommon macroscopic magnetic properties in magnetic field up to 9 T.

Specific heat studies were chosen as the main tool for realizing the former task, because specific heat is very sensitive to phase transitions of all physical nature, i.e., its value changes rapidly near all phase transitions.

For realizing the latter task: (i) the parallel to the applied magnetic field, **B**, component of mass magnetization, **M** (expressed in A m^2 kg^{-1}), and (ii) the magnetic torque:

$$\boldsymbol{\tau} = m \cdot \mathbf{M} \times \mathbf{B}, \tag{1}$$

proportional to the sample mass, m (in our case $m =$ 0.479 mg), and to the perpendicular to **B** component of **M**, were measured for **B** rotating in the a-c and b-c planes, as functions of an angle defining orientation of **B** within these planes, for several fixed temperature, T, and B values (up to 9 T). Near T_N and T_{N1}, the angular functions were measured each 0.1 or 0.2 K.

Moreover, dc magnetic susceptibility along the a, b, and c axes was measured as a function of temperature for B ranging from 1 to 9 T. For convenience, we call "magnetic susceptibility" the quantity $\chi = M/B$, not M/H, all over the text.

The specific heat, magnetic torque and dc susceptibility were measured by using the PPMS system (Quantum Design) equipped with the 9-T superconductive magnet and the heat capacity, torque and vibrating sample magnetometer, VSM, options. The magnetization as a function of orientation of **B** was measured by using the SQUID magnetometer (Quantum Design) equipped with the sample rotator and 5-T magnet.

The $LiNiPO_4$ single crystals studied were provided by the group of H. Schmid at the University of Geneva. They were grown by using the method of growth from the solution, described in Ref. [25]. A polycrystalline powder $LiNiPO_4$ sample, for which specific heat was studied, was prepared by a standard ceramic high-temperature method [26].

III. SPECIFIC HEAT OF $LiNiPO_4$ SINGLE CRYSTAL

The total specific heat C_p of the single crystalline sample of a mass of 4.053(1) mg was measured by using the relaxation method, Fig. 2(a), over the temperature range from 2.5 to 300 K for zero magnetic field, and from 2.5 to 50 K for fixed, nonzero B values, since it was verified that above 50 K, the influence of B on the specific heat was negligible. The experimental points were taken each ∼0.2 K below 50 K and each ∼10 mK or even denser near the phase transitions, and each 5 K for $T > 50$ K. The lattice specific heat C_l, plotted with the red solid line in Fig. 2(a), was estimated by mixing the Debye and Einstein models, according to the formula

$$C_l(T) = \frac{k_B N_A}{(1-\alpha T)}\left[3n_D\left(\frac{T}{\theta_D}\right)^3 \int_0^{\frac{\theta_D}{T}} \frac{x^4 e^x}{(e^x-1)^2}dx + \sum_{i=1}^{n_O} n_i \left(\frac{\theta_i}{T}\right)^2 \frac{e^{\frac{\theta_i}{T}}}{(e^{\frac{\theta_i}{T}}-1)^2}\right], \tag{2}$$

where k_B, N_A, θ_D, n_D, n_O, θ_i, and n_i denote, respectively, the Boltzmann's constant, the Avogadro's number, the Debye temperature, the number of modes considered within the Debye model, the number of nondispersive optical branches treated within the Einstein model, energy of the ith Einstein's branch (expressed in temperature units), and the number of optical modes assigned to the ith branch. Additionally, the

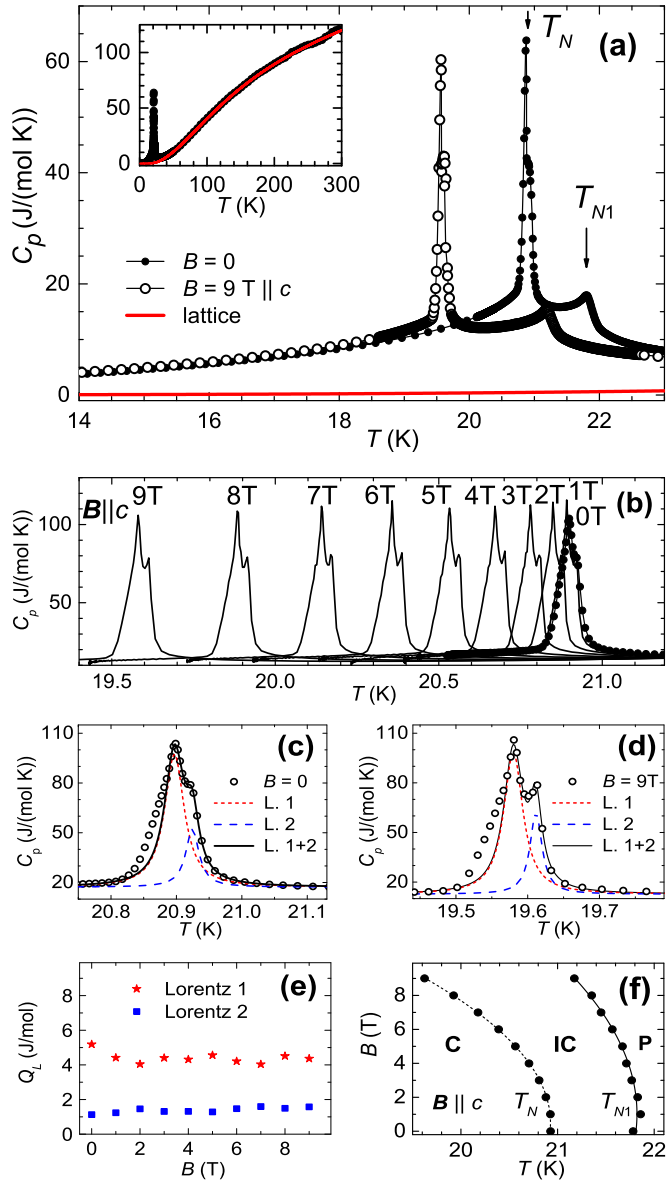

FIG. 2. Specific heat C_p of the $LiNiPO_4$ single crystal. (a) C_p as a function of temperature, T, near the two magnetic phase transitions, for $B = 0$ and 9 T parallel to the c axis. Anomalies related to the second-order transition between the P and IC phases, and to the first-order transition between the IC and C phases appear for $B = 0$ at T_{N1} and T_N, respectively. Inset shows $C_p(T)$ up to 300 K in $B = 0$. The estimated lattice contribution is plotted with the red solid line. (b) Evolution of the split anomaly related to the IC-C transition under influence of B parallel to the c axis, determined by using the "slope analysis procedure" (full circles for $B = 0$ and solid lines for $B \neq 0$). (c) Decomposition of the IC-C anomaly into two Lorentz functions for $B = 0$ and (d) for $B = 9$ T. (e) The area below each of the Lorentz functions as a function of B. (f) Phase diagram for $B \leqslant 9$ T, parallel to the c axis. The fitted functions $T_N(B)$ and $T_{N1}(B)$ are plotted with the dotted and solid line, respectively.

condition $n_D + \sum_{i=1}^{n_O} n_i \leqslant 21$ obeys. Since both the Debye and the Einstein model were elaborated for the systems of constant volume, whereas the measurements were performed at constant pressure, the factor $1/(1-\alpha T)$ was introduced, which, according to the model proposed in Ref. [27], describes the increase of the phonon specific heat related to thermal expansion of the crystal lattice. Equation (2) was fitted to the experimental points measured above 40 K, because for these temperatures, C_l is the only significant contribution to the specific heat. When fitting, energies of four optical modes, selected from all determined in Ref. [25] as the most influencing the temperature dependence of specific heat, were taken as known parameters, whereas θ_D, n_D, n_i, and α were fitted. The best description of the phonon specific heat of $LiNiPO_4$, plotted in Fig. 2(a) with the red line, was achieved for the following values of the parameters: $\alpha = 0.0007$ K^{-1}, $\theta_D =$ 385 K, $n_D = 2$, $\theta_1 = 122$ cm^{-1} ($\approx$175.5 K), $n_1 = 2$, $\theta_2 =$ 262 cm^{-1} ($\approx$377 K), $n_2 = 4$, $\theta_3 = 329$ cm^{-1} ($\approx$473.4 K), $n_3 = 2$, $\theta_4 = 515$ cm^{-1} ($\approx$741 K), $n_4 = 4$.

In all the measured curves, two qualitatively different anomalies, i.e., the high narrow peak at T_N, accompanying the first-order transition from the C to the IC phase, and the smaller, wider and asymmetric maximum of the λ-type at T_{N1}, accompanying the second-order transition from the IC to the paramagnetic, P, phase, were observed. Actually, P is not the purely paramagnetic phase and short-range spin correlations are present in it up to ~36 K [18,21]. Since the C–IC phase transition is very sharp and occurs within a narrow temperature range, the relaxation method of measurement is not well suited for studying it. As it was explained, e.g., in Ref. [28], the relaxation method, in which the heat capacity value averaged over a temperature range covered by the measuring pulse is determined, deforms an anomaly accompanying a narrow first-order transition. Moreover, due to overheating and overcooling phenomena, the anomaly is deformed in different way when the measurements are carried on heating and on cooling the sample. The "bump" on the high-temperature side of the anomaly accompanying the IC–C transition, registered by means of the standard relaxation method, Fig. 2(a), suggested this anomaly to be a superposition of two anomalies. Thus, it was studied in detail by using the "slope analysis procedure," implemented recently in the heat capacity PPMS option [29], to facilitate studies of phase transitions occurring in a temperature range narrower than that covered by a measuring pulse. In this procedure, a dependence of heat capacity on temperature, T, for a range covered by a single measuring pulse is determined by calculating the derivative dT/dt, where t denotes time, and using the formula

$$C_{\text{total}}(T) = \frac{-K_w(T(t) - T_b) + P(t)}{dT/dt}, \tag{3}$$

where C_{total}, K_w, $P(t)$, and T_b denote, respectively, the total heat capacity of the calorimeter with the sample, thermal conductivity of the wires connecting the calorimeter with the calorimeter case, time dependence of power supplied to the calorimeter during the measuring pulse, and the temperature of the calorimeter case. Equation (3) is analogous to that applied in the "continuous heating" method of specific heat measurement. The sample heat capacity is calculated by subtracting the addenda heat capacity, measured earlier, from C_{total}. The possibility of precise determining a shape of an anomaly related to a first-order transition is the main advantage of this procedure. However, due to uncertainty of determination of dT/dt, the absolute specific heat values, especially those found for temperatures close to the beginning and the end of the heating pulse, and to the end of the measurement cycle, are not so accurate as those determined by using the standard relaxation procedure, which is the drawback of the slope analysis procedure.

When applied to the IC–C phase transition, the slope analysis procedure showed, Figs. 2(b)–2(d), that the specific heat anomaly is actually narrower (i.e., ~60 not ~100 mK at the half of height) and higher [103.9 not 63.8 J mol^{-1} K^{-1} in peak] than that registered by using the standard method, and that it is really split into two maxima. Thus, we conclude that we deal with two coupled first-order transitions. One of them is, obviously, the magnetic IC-C transition, whereas the other one we suppose to be the transition to the ferroelectric phase. However, in order to verify this interpretation, the precise electric polarization measurements, not available in our laboratory, would be necessary. Since both overlapping transitions are of the first-order, as observation of a small temperature hysteresis (~10 mK) of appearance of the anomaly at measurements on heating and on cooling confirmed, we assumed that the shape of each anomaly can be approximated by the Lorentz function L. Then, the measured anomaly was decomposed into two Lorentzian components:

$$C_p(T) = C_0 + \sum_{i=1}^{2} L\left(T, T_L^i, y_0^i, w^i\right),$$

$$L(T, T_L, y_0, w) = y_0 \frac{w^2}{4(T - T_L)^2 + w^2}, \tag{4}$$

where C_0 is the (mainly phonon) background above which the anomaly rises up, whereas y_0 is the maximum value at T_L and w is the half-width of the Lorentz function. The integral of the L function (4) taken from minus to plus infinity: $Q_L = w y_0 \pi/2$, can be interpreted as estimation of the latent heat related to the considered phase transition. As Figs. 2(c) and 2(d) illustrate, the high-temperature side of the measured anomaly can be approximated nearly perfectly with the two Lorentz functions. Splitting between the centers of the Lorentz functions is equal to ≈27 mK in zero field and increases approximately linearly with B directed along the c axis to ≈32 mK at 9 T, whereas the latent heat Q_L of each component remains practically independent of B, Fig. 2(e).

The measurements of specific heat as a function of temperature proved that the magnetic field up to 9 T, when applied along the b or a axis, does not influence the temperatures of the C-IC and IC-P transitions. However, when the field is applied along the c axis, it shifts the temperatures of both transitions towards lower temperatures. This is consistent with the published phase diagram [9,20], however, the present detailed studies for $B \leqslant 9$ T showed that both phase transition temperatures are, approximately, the parabolic functions of B, Fig. 2(f):

$$T_{N1}(B) = 21.84 - 0.008\,B^2,$$
$$T_N(B) = 20.92 - 0.0165\,B^2. \tag{5}$$

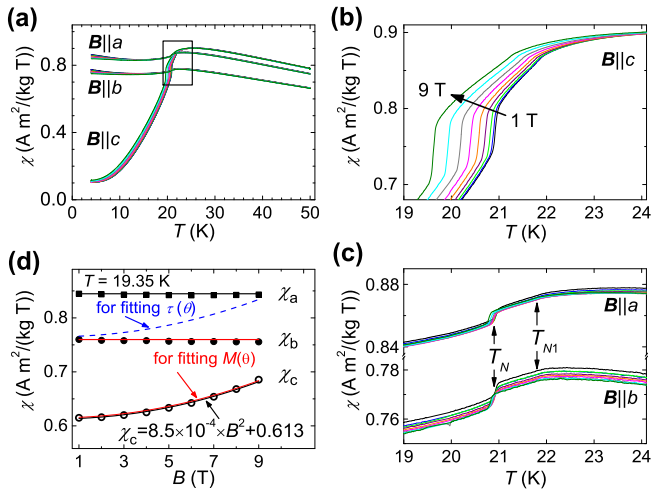

FIG. 3. Magnetic susceptibility of $LiNiPO_4$, defined as $\chi = M/B$, measured along the a, b, and c axes at fixed $B = 0, 1, 2, \ldots, 9$ T values, as a function of temperature. (a) Results for $T \leqslant 50$ K. (b) χ_c and (c) χ_a and χ_b in the phase transition region, indicated in (a) by the rectangle. (d) χ along the a, b, and c axes as a function of B at $T = 19.35$ K. The dashed blue and solid red lines present the functions used to fit the $M(\theta)$ and $\tau(\theta)$ functions according to the third hypothesis.

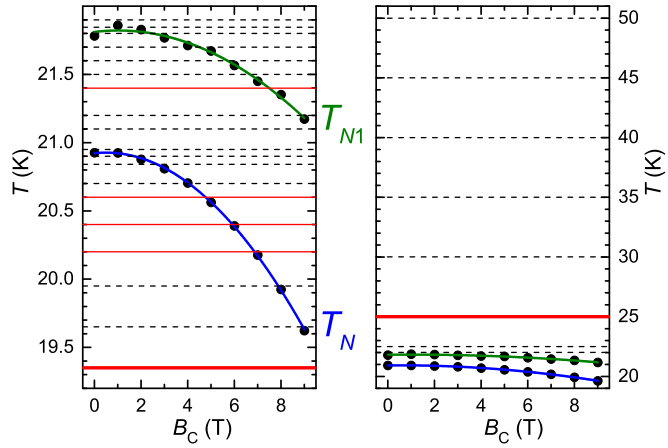

FIG. 4. Phase diagram of $LiNiPO_4$ for magnetic field parallel to the c axis, B_c. Temperatures for which the torque and magnetization were measured as a function of θ, are denoted with horizontal lines. The red solid lines distinguish those temperatures for which the data are presented in Figs. 5 (thick lines) and 6 (thin lines).

In conclusion, the specific heat studies of the $LiNiPO_4$ single crystal showed the discontinuous IC-C phase transition to be in fact a pair of the coupled first order transitions, one of which is the magnetic one and the other one is possibly the ferroelectric one. Moreover, they allowed to determine precisely the shape of the phase diagram for the magnetic field $B \leqslant 9$ T parallel to the c axis.

IV. TORQUE AND MAGNETIZATION STUDIES

In order to study macroscopic magnetic properties of the $LiNiPO_4$ single crystals, (i) magnetization was measured as a function of temperature for several values of **B** oriented along the a, b, and c axes, Fig. 3, and (ii) torque and magnetization were measured as a function of orientation of **B** for **B** rotating within the a-c and b-c planes, for several fixed B values and 28 fixed temperature values, indicated in Fig. 4 with horizontal lines. The functions measured at the temperatures 19.35 and 25 K (indicted in Fig. 4 with the thick red solid lines), distant from the temperatures of magnetic phase transitions, are presented in Fig. 5, whereas the ones measured at four intermediate temperatures, selected as the most informative and indicated in Fig. 4 with thin red solid lines, are presented in Fig. 6. In all the figures, the same convention of presenting the data is used. That means, orientation of the magnetic field within the a-c and b-c planes is determined by the angle θ counted from the c axis, i.e., $\theta = 0^\circ$ corresponds to the orientation along the c axis, whereas $\theta = 90^\circ$ corresponds to the a (b) axis for the a-c (b-c) plane. The panels I and II present the torque versus θ functions for magnetic field rotating within the a-c and b-c planes, respectively. The panels III present the sets of magnetization versus θ functions. Pairs of the functions measured at the same B for the a-c and b-c planes, touching for $\theta = 0^\circ$, 180°, and 360° values corresponding to the c axis, are shifted along the y axis by the values given above them near $\theta = 0^\circ$, in order to maintain legibility. Experimental points for the a-c and b-c planes are plotted with full circles and triangles, respectively. Theoretical functions calculated in frames of the model that we propose below are plotted with solid lines for the functions for which the experimental data were available and with dashed lines for the cases in which the experimental data were lacking and these are the theoretical simulations only.

Figure 5 illustrates a general form of the dependence of magnetic torque on the orientation of magnetic field within the a-c and b-c planes of the orthorhombic $LiNiPO_4$ crystal for temperatures distant from the phase transitions. Generally, with accuracy to a constant positive or negative multiplier, the torque should consequently do the following: (1) grow from zero value at $\theta = 0$ to a certain maximum value $\tau_{\max}$ at $\theta = \alpha$, where $0 < \alpha < 90^\circ$, (2) then, fall down to zero at $\theta = 90^\circ$, (3) change its sign and fall down to the minimum value $-\tau_{\max}$ at $\theta = 180^\circ - \alpha$, (4) grow and reach zero value at $\theta = 180^\circ$, (5) change its sign and grow to $\tau_{\max}$ at $180^\circ + \alpha$, (6) fall down, reaching zero at $\theta = 270^\circ$, (7) change its sign and fall down reaching $-\tau_{\max}$ at $\theta = 360^\circ - \alpha$, and (8) grow and reach zero value at $\theta = 360^\circ$.

Thus the measured angular functions should repeat with the period of 180°. Since presence of a constant nonzero bias value of the signal and of small slackness of mechanical elements of the horizontal rotator of the sample are inherent imperfections of the torque magnetometer option, at first, the constant bias was subtracted from the raw experimental data and then, the data were symmetrized for the period of 180° by using the formula:

$$\tau(\theta, B) = \frac{\tau_m(\theta, B) + \tau_m(\theta + 180^\circ, B)}{2}, \qquad (6)$$

where τ_m is the measured value after subtracting the bias and τ is the symmetrized torque, plotted in Figs. 5 and 6.

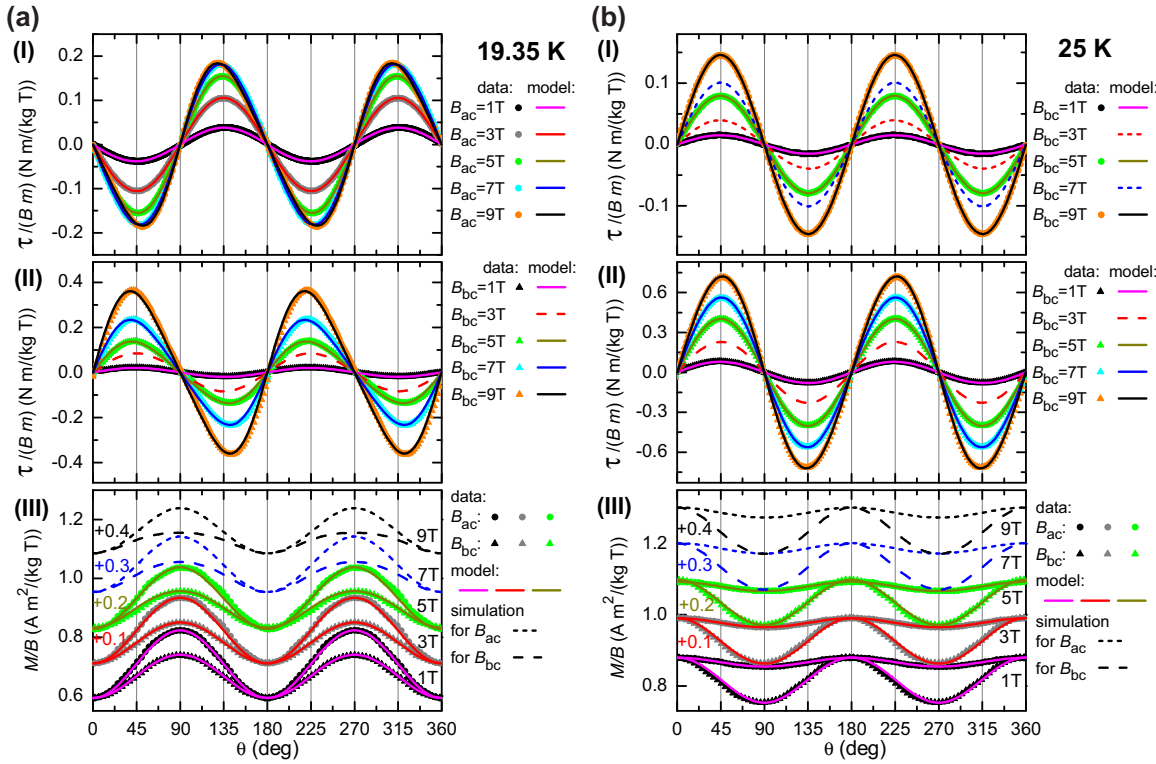

FIG. 5. Magnetic torque for **B** rotating within the *a*-*c* (I) and *b*-*c* (II) planes and magnetization (III) for **B** rotating within the *a*-*c* (upper curves) and *b*-*c* (bottom curves) planes plotted as a function of orientation θ of **B** within the appropriate plane for $LiNiPO_4$ at (a) $T = 19.35$ and (b) 25 K.

The shapes of magnetization versus θ functions are dominated by two factors, i.e., by the dependence of susceptibility along the main crystallographic axes on temperature, Fig. 3, and by the fact that only the parallel to the *c* axis component of *B* influences the temperatures T_N and T_{N1}, Fig. 4. Thus, at 19.35 K, Fig. 5(a), which is the temperature lower than T_N even in the field of 9 T, and at which $\chi_c < \chi_b < \chi_a$, the $M(\theta, T, B{=}\text{const.})$ functions reach their maxima at $\theta = 90^\circ$ and 270°, i.e., for the *a* axis for the *a*-*c* plane, and for the *b* axis for the *b*-*c* plane. However, the maximum magnetization value for the *a* axis is larger than that for the *b* axis. On the contrary, at 25 K, Fig. 5(b), which is the temperature greater than T_{N1}, Fig. 4, the inequality $\chi_b < \chi_a < \chi_c$ obeys and maxima of the $M(\theta, 25\,\text{K}, B = \text{const.})$ functions appear for the *c* axis ($\theta = 0^\circ, 180^\circ$, and 360°), whereas the deepest minima appear for the *b* axis for *B* rotating within the *b*-*c* plane and the shallow minima appear for the *a* axis for *B* rotating within the *a*-*c* plane. More peculiar behaviors appear for those temperatures and *B* values, for which the magnetic field of a certain orientation induces the phase transitions. For example, at 20.6 K, Fig. 6(c), $B \geqslant 4.8$ T directed along the *c* axis induces the transition to the IC phase. Thus, the $M(\theta,\ 20.6\,\text{K}, B = \text{const.})$ functions measured for $B \leqslant 3$ T have a shape characteristic of low-temperature antiferromagnetic C phase, like those presented in Figs. 5(a) and 6(b). The functions measured for $B = 5$ T, have the "low-temperature" shape only for the field orientation ranges $\sim 45^\circ < \theta < \sim 135^\circ$ and $\sim 225^\circ < \theta < \sim 315^\circ$, for which the parallel to the *c* axis component of the field is smaller than 4.8 T and the sample remains in the low-temperature C phase. For the orientation ranges $\sim(-45^\circ) < \theta < \sim 45^\circ$ and $\sim 135^\circ < \theta < \sim 225^\circ$, the sample undergoes the phase transition to the IC phase and the $M(\theta, 20.6\,\text{K}, 5\,\text{T})$ functions resemble those appearing within the IC phase, e.g., those presented in Fig. 6(d) for $T = 21.4$ K.

The magnetic torque versus θ functions are more peculiar and cannot be fully explained by the evolution of the relation between susceptibilities along the main axes. At low temperature, $\chi_c < \chi_b < \chi_a$, and for $\theta = 45^\circ$, the magnetic torque should be negative for **B** lying within the *a*-*c* plane and positive for **B** lying within the *b*-*c* plane, and, as Fig. 5(a) illustrates, the experimental results agree with this expectation. However, when the temperature increases the relation between susceptibilities changes to $\chi_b < \chi_a < \chi_c$ and change of the sign of the torque for $\theta = 45^\circ$ is expected for both planes. The torque measured for the *a*-*c* plane fulfills this expectation, Fig. 6, in particular, with increase of *T*, the $\tau(\theta, T, B)$ values decrease, then, when *T* reaches the region in which the field-induced phase transitions take place, the shape of the $\tau(\theta, T, B)$ curves modifies strongly, for example doubling of the angular period of τ appears for $B = 9$ T and $T = 20.2$ K, Fig. 6(a). When temperature reaches 20.4 K, the torque changes its sign in high field, Fig. 6(b), and then, for higher temperatures, up to 50 K, i.e., up to the highest temperature at which measurements were done, the τ versus θ functions have a shape similar to that observed at low temperatures for all *B* values but the sign of the torque is opposite. In contrast to this behavior, the $\tau(\theta, T, B)$ curves measured for the field rotating within the *b*-*c* plane have the

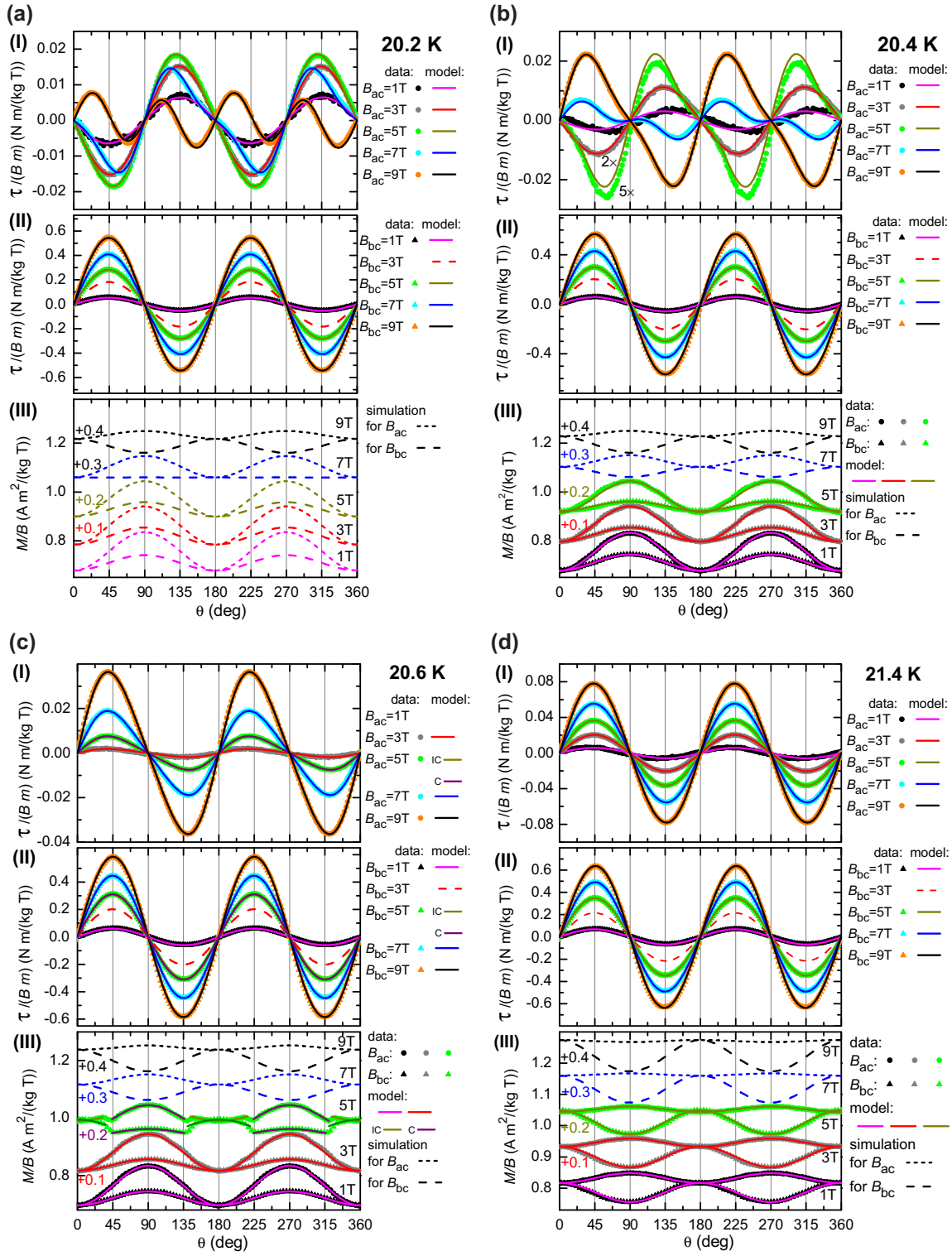

FIG. 6. Magnetic torque for **B** rotating within the *a*-*c* (I) and *b*-*c* (II) planes and magnetization (III) for **B** rotating within the *a*-*c* (upper curves) and *b*-*c* (bottom curves) planes, plotted as a function of orientation θ of **B** within the appropriate plane for $LiNiPO_4$ at (a) 20.2, (b) 20.4 (due to small torque values in the *a*-*c* plane, the functions for $B = 3$ and 5 T were multiplied by 2 and 5, respectively), (c) 20.6, and (d) 21.4 K.

same shape over the whole temperature range studied and do not experience the expected changes.

There is also one more signature of uncommon properties of $LiNiPO_4$. If the orthorhombic $LiNiPO_4$ crystal behaved like a standard linear medium showing different, field-independent susceptibilities along the three main axes, the torque for the *a*-*c* and *b*-*c* planes would be proportional to $\sin(2\theta)$ and the angle α defined above would be equal to 45°. However, for majority of the measured functions, α is different from 45°. We considered four possible explanations of this effect.

As the first hypothesis, we assumed this to be the artifact related to "circumferential backlash" of mechanical system of the horizontal rotator, which can be eliminated by averaging the τ values with the use of the expression:

$$\tau_{av}(\theta, B) = \frac{\tau(\theta, B) - \tau(\theta + 90^\circ, B)}{2}. \quad (7)$$

For the $\tau_{av}(\theta, B)$ functions, α was really equal to 45° but, as we verified, in order to fit theoretical functions to the experimental $\tau_{av}(\theta, B)$ curves, it was necessary to take χ_a, χ_b, and χ_c values unacceptably, i.e., by ≈30%, different from the values measured with the VSM magnetometer. Thus we rejected this interpretation and realized that for $LiNiPO_4$, the α values are really different from 45°.

As the second hypothesis, we considered the microscopic model, i.e., the magnetic moments of four sublattices, their interaction with the applied field **B**, and the parameters describing their magnetocrystalline anisotropy and the exchange interactions between them [9,10,20], Table I. Then, we tried to minimize the free energy of this system for different orientations of **B**, with respect to orientations of the magnetic moments of particular sublattices. Unfortunately, it turned out that this problem is not stable numerically and has too many free parameters. It was not possible to determine a unique set of orientations of the magnetic moments of all sublattices, determining unequivocally the torque and the net magnetic moment along **B**. Thus we realized that the phenomenological approach will be more effective.

As the third hypothesis, we assumed that $\alpha \neq 45^\circ$ values are related to the parabolic dependence of χ_c on B_c. As illustrates Fig. 3(d), for $T = 19.35$ K, after converting the susceptibility versus temperature curves, measured for different B values, into the $\chi_i(B_i, T = \text{const.})$ functions, where i denotes the axis a, b, or c along which the field was applied and the susceptibility was measured, one realizes that χ_a and χ_b are practically independent of field, whereas χ_c depends parabolically on B_c. We verified that taking the parabolic $\chi_c(B_c)$ dependence and the measured χ_a and χ_b values it was not possible to reproduce simultaneously the measured τ and M versus θ functions. It was necessary to take substantially, i.e., by ≈30%, different $\chi_c(B_c)$ functions to get a perfect description of the experimental $M(\theta)$ and $\tau(\theta)$ curves. For example, for $T = 19.35$ K, a good description of the angular M dependence for the a-c plane was obtained with the use of the measured $\chi_c(B_c)$ dependence, plotted in Fig. 3(d) with the red solid line, whereas the perfect description of the angular τ dependence was achieved with the use of the dependence, plotted in Fig. 3(d) with the dashed blue line, shifted by ≈25% with respect to the measured one. Thus, we realized that it is not possible to obtain a consistent description of the experimental data by taking into account the parabolic dependence of χ_c on B_c, hence, this dependence is not responsible for the appearance of the $\alpha \neq 45^\circ$ values.

In conclusion, we realized that the presence of the $\alpha \neq 45^\circ$ values is not the artifact and that it is related to any uncommon, not reported till now effect. We called it "off-diagonal nonlinear magnetic susceptibility" and proposed the following fourth hypothesis to describe it. Since the four-sublattice antiferromagnetic structure of $LiNiPO_4$ with a small canting of magnetic moments of the particular sublattices appears as the result of the complex exchange interactions, we assumed that the magnetic susceptibility along each of the main crystallographic axis depends not only on the parallel to this axis component of the applied field **B** but also on the perpendicular to this axis component of **B**. However, due to the orthorhombic symmetry of the crystal, this can not be a simple linear dependence, which is odd with respect to the perpendicular component, but it must be a function even with respect to the sign of the perpendicular **B** component. Since the modulus and the square functions are the simplest of them, we chose arbitrarily the square function. Thus, using the coordinate system coupled to the main crystalline axes and denoting the parallel to the particular axes components of all vectors by the respective subscripts, we obtain that **M** induced by **B** rotating within the a-c plane is given by the formula:

$$\begin{bmatrix} M_a \\ M_b \\ M_c \end{bmatrix} = \begin{bmatrix} [\chi_a + \chi_{ac}(B\cos\theta)^2]B\sin\theta \\ 0 \\ [\chi_c + \chi_{ca}(B\sin\theta)^2]B\cos\theta \end{bmatrix}, \quad (8)$$

and **M** induced by **B** rotating in the b-c plane equals to

$$\begin{bmatrix} M_a \\ M_b \\ M_c \end{bmatrix} = \begin{bmatrix} 0 \\ [\chi_b + \chi_{bc}(B\cos\theta)^2]B\sin\theta \\ [\chi_c + \chi_{cb}(B\sin\theta)^2]B\cos\theta \end{bmatrix}. \quad (9)$$

Then, the expressions describing the parallel to **B** component of **M** and the magnetic torque τ take the form

$$M_{||}^{ac}(\theta, B) = \mathbf{M}\cdot\frac{\mathbf{B}}{B} = (\chi_a \sin^2\theta + \chi_c\cos^2\theta)B + \frac{\chi_{ac} + \chi_{ca}}{4}\sin^2 2\theta\, B^3, \quad (10)$$

$$\tau_b(\theta, B) = m(\mathbf{M}\times\mathbf{B})_b = m\sin 2\theta\, B^2 \times \left(\frac{\chi_c - \chi_a}{2} + \frac{\chi_{ca}\sin^2\theta - \chi_{ac}\cos^2\theta}{2}B^2\right), \quad (11)$$

for **B** rotating in the a-c plane (and $\tau||b$), and the form

$$M_{||}^{bc}(\theta, B) = \mathbf{M}\cdot\frac{\mathbf{B}}{B} = (\chi_b \sin^2\theta + \chi_c\cos^2\theta)B + \frac{\chi_{bc} + \chi_{cb}}{4}\sin^2 2\theta\, B^3, \quad (12)$$

$$\tau_a(\theta, B) = m(\mathbf{M}\times\mathbf{B})_a = m\sin 2\theta\, B^2 \times \left(\frac{\chi_b - \chi_c}{2} - \frac{\chi_{cb}\sin^2\theta - \chi_{bc}\cos^2\theta}{2}B^2\right), \quad (13)$$

for **B** rotating in the b-c plane (and $\tau||a$).

Next, we fitted the derived (10)–(13) formulas to the experimental data. Since the procedures applied for **B** rotating within the a-c and b-c planes were analogical, below, only the case of the a-c plane is described. For **B** rotating within the a-c plane, for each of the fixed temperatures, denoted in Fig. 4 with the horizontal lines, we took the measured χ_a, Fig. 3, as the starting value and fitted the function (10) to the measured angular $M(\theta, B, T)$ dependence, treating χ_c and the sum $(\chi_{ac} + \chi_{ca})$ as the fitted parameters. Next, we used χ_a and the found χ_c as known parameters and fitted the χ_{ac}

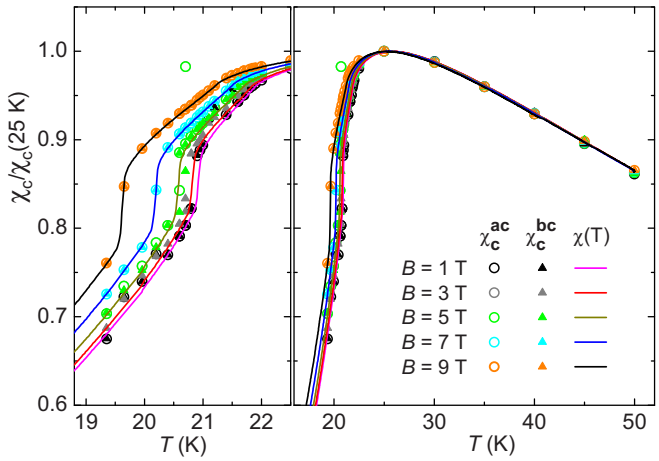

FIG. 7. Normalized susceptibility along the c axis as a function of temperature, measured with VSM (solid lines) and found by fitting the model to the measured M and τ vs θ curves for the a-c (circles) and b-c (triangles) planes. The 0.880, 0.891, 0.893, 0.901, and 0.902 A m^2 kg^{-1} T^{-1} normalizing values measured at 25 K for 1, 3, 5, 7, and 9 T, respectively, were used.

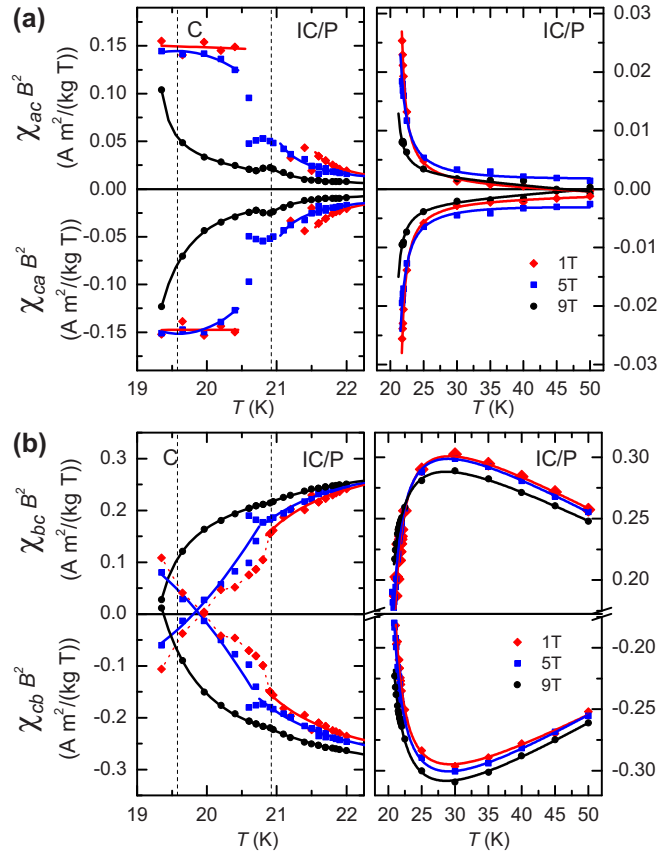

FIG. 8. Products of B^2 and the coefficients of the off-diagonal components of susceptibility (symbols), found by fitting the model to the experimental data, as a function of temperature for the (a) a-c and (b) b-c planes. Solid lines present the results of fitting (14) to these curves.

and χ_{ca} values to get the best fit of the (11) function to the experimental $\tau_b(\theta, B, T)$ dependence. Since the sum of the χ_{ac} and χ_{ca} determined in the latter step was usually not equal exactly to the $(\chi_{ac} + \chi_{ca})$ parameter determined in the former step, we verified that in all the cases, the replacement of this parameter with $\chi_{ac} + \chi_{ca}$ led to no noticeable difference. In order to get a consistent theoretical description of the experimental curves, it was necessary to modify slightly, usually to decrease by circa 0.1%–4%, the starting χ_a value. Also the fitted χ_c values were slightly, by up to 3%, different from the measured ones, Fig. 7. We attribute this slight discrepancy of the measured and fitted χ_i values ($i = a$, b, and c) to the fact, that we compared the functions measured in three experimental devices and it was quite natural that the temperatures reported by each of them as the same temperature were actually slightly different. This was visible clearly near the phase transitions, where even the differences ~10 mK were noticeable and the larger modifications were needed, e.g., for the b-c plane, $T = 20.7$ K, and $B = 3$ T, the χ_b value had to be decreased by 9.5%.

Thus, the theoretical functions describing the experimental data the best, plotted in Figs. 5 and 6 with solid lines, were calculated by using: the slightly modified χ_a and χ_b parameters; χ_c found by fitting $M(\theta, B, T)$ (equal to the measured χ_c with accuracy to 3%); χ_{ac} and χ_{ca} or χ_{bc} and χ_{cb} found by fitting $\tau(\theta, B, T)$. For those B values for which the $M(\theta)$ or $\tau(\theta)$ functions were not measured, the theoretical curves were mimicked by using parameters estimated based on the values found for other B values. The simulated curves are plotted in Figs. 5 and 6 with dashed lines. For temperatures close to T_N and T_{N1}, where the sample was in different magnetic phases for different ranges of θ, the fitting was performed separately for θ ranges corresponding to different phases, Fig. 6(c). We fitted the (10)–(13) functions to all the curves measured at 28 fixed temperatures, Fig. 4, and achieved a very good, i.e., not worse than that presented in Figs. 5 and 6, agreement between the experimental and the theoretical functions for nearly all cases, with exception of the curves measured in $B = 1$ T at 20.6 and 20.95 K, where the torque was very small, on the level of noise.

Products of B^2 and the determined coefficients of the off-diagonal susceptibility are plotted in Fig. 8 as a function of temperature. We found that these curves, with exception of $\chi_{bc}B^2$ and $\chi_{cb}B^2$ in the C phase, can be described very well by the sum of the linear, constant, and hyperbolic functions:

$$F(T, \nu_1, \nu_2, \nu_3, \nu_4) = \nu_2(T - \nu_1) + \nu_3 + \frac{\nu_4}{T - \nu_1}. \quad (14)$$

The determined ν_i values ($i = 1$–4) are given in Table II.

In conclusion, the detailed studies of the M and τ versus θ functions, in particular, establishing that τ extrema appear at the angles different from the odd multiples of 45°, revealed existence of the off-diagonal nonlinear contribution to the magnetic susceptibility, i.e., of the effect, that the susceptibility along each of the three main crystallographic axes has a component proportional to the square of the perpendicular to this axis component of B. The very good agreement between the derived theoretical functions (10)–(13) and the experimental ones is a strong argument in favor of this interpretation. In our opinion, this effect was overlooked, because in the previous studies, the susceptibility was measured for B applied

TABLE II. Parameters fitting the function (14) to the $\chi_{ij}(T, B)\, B^2$ curves. Uncertainty of the last digit of each parameter, estimated as the range for which the quality of the fit does not deteriorate evidently, when all other parameters are fixed, is given in parentheses.

	ν_1 (K)	$\nu_2\left(\frac{Am^2}{\mathrm{kg\,T\,K}}\right)$	$\nu_3\left(\frac{\mathrm{Am^2}}{\mathrm{kg\,T}}\right)$	$\nu_4\left(\frac{\mathrm{Am^2\,K}}{\mathrm{kg\,T}}\right)$	$\frac{B}{(\mathrm{T})}$
		Temperature range of the *C* phase			
$\chi_{ac}\, B^2$	−20(5)	0.00010(2)	−0.152(1)	0	1
	0	0.74682(7)	−29.434(1)	287.03(2)	5
	18.76(2)	−0.0127(7)	0.052(1)	−0.097(2)	9
$\chi_{ca}\, B^2$	−4.6(2)	−0.00284(3)	0.218(1)	0	1
	0	−0.53992(3)	21.240(2)	−206.05(2)	5
	19.18(2)	−0.0083(15)	0.023(1)	0.013(1)	9
$\chi_{bc}\, B^2$	0	0	0	0	1
	0	0.9666(2)	−35.473(5)	323.6(1)	5
	18.93(3)	0.014(2)	0.231(7)	−0.085(5)	9
$\chi_{cb}\, B^2$	0	0	0	0	1
	0	−0.9215(2)	33.47(5)	−300.65(15)	5
	18.5(3)	0.028(2)	−0.439(5)	0.36(1)	9
		Temperature range of the *IC* and *P* phases			
$\chi_{ac}\, B^2$	21.1(2)	0.000020(5)	−0.0013(1)	−0.017(1)	1
	20.6(1)	−0.00003(1)	−0.0015(2)	−0.022(1)	5
	20.5(3)	0.00008(1)	−0.0020(2)	−0.010(1)	9
$\chi_{ca}\, B^2$	21.0(1)	−0.000040(1)	0.00012(4)	0.0178(4)	1
	20.5(2)	0.000020(3)	0.00052(5)	0.0215(5)	5
	20.5(1)	−0.000090(2)	0.00197(5)	0.0080(5)	9
$\chi_{bc}\, B^2$	19.4(2)	−0.00300(5)	0.359(1)	−0.28(1)	1
	19.19(6)	−0.00303(5)	0.360(2)	−0.3(1)	5
	18.6(1)	−0.00275(7)	0.344(2)	−0.270(15)	9
$\chi_{cb}\, B^2$	19.45(5)	0.00287(2)	−0.351(1)	0.28(1)	1
	19.15(5)	0.00325(5)	−0.366(1)	0.32(1)	5
	18.6(1)	0.00325(5)	−0.374(2)	0.325(15)	9

along the main crystallographic axes, when the perpendicular to these axes component of B was zero. Thus only the angular measurements performed now allowed to reveal the presence of the off-diagonal components of susceptibility.

V. SPECIFIC HEAT OF $LiNiPO_4$ POWDER

Temperature dependence of specific heat of the $LiNiPO_4$ polycrystalline powder was measured for $B = 0$ and 9 T by using an aluminum crucible (this method of measuring powders was proposed in Ref. [30]) and the standard procedure of the HC option of PPMS. Outside the range of phase transitions, the $C_p(T, B = \text{const.})$ functions for the powder agree well with the ones measured for the single crystal, Fig. 9. However, inside this range, the anomalies accompanying the phase transitions in the powder are wider, lower, and evolving under influence of B in a different way than the ones appearing for the single crystal. We attributed the former effect (i.e., smearing of the anomaly) to the presence of a distribution of the phase transition temperatures in the powder. In principle, such distribution could be related to the size effect, i.e., to the reported in Ref. [31] dependence of the magnetic transition temperature on the size of nanograins of nanopowder. However, the performed SEM studies showed that the mean size of grains of our powder was $\sim$1.7 μm, therefore, the size effect was negligible in this case. Thus, taking into account that the integral of the measured powder specific heat over temperature interval from 2 to 24 K is smaller by $\approx$5% than the analogous integral for the single crystal, we assumed that the regions close to surfaces of particular powder grains can have different thermal and magnetic properties than the interior of the grains, which leads to a distribution of the transition temperatures. These differences can be attributed to Li vacancies and to point defects, like interstitial Ni and Ni in Li sites. To perform quantitative analysis of the observed effects, we assumed the lattice contribution to the powder specific heat to be the same as in the single crystal (2), we subtracted it from the total specific heat, and determined the nonphonon contribution to the specific heat of the powder. Then, we assumed that for each region showing the transition temperatures t_N and t_{N1} different than T_N and T_{N1}, the temperature dependence of the nonphonon specific heat $C_M^{t_N}(T)$ has the same shape as for the ideal single crystal, $C_M(T)$, but it is shifted along the T axis by such a value that the specific heat maximum appears at t_N, i.e.,

$$C_M^{t_N}(T) = C_M(T - (t_N - T_N)), \tag{15}$$

where $T_N = 20.875$ K denotes the temperature at which maximum specific heat was measured for the single crystal by using the standard method. Next, we assumed that the mass distribution of regions of different transition temperatures is

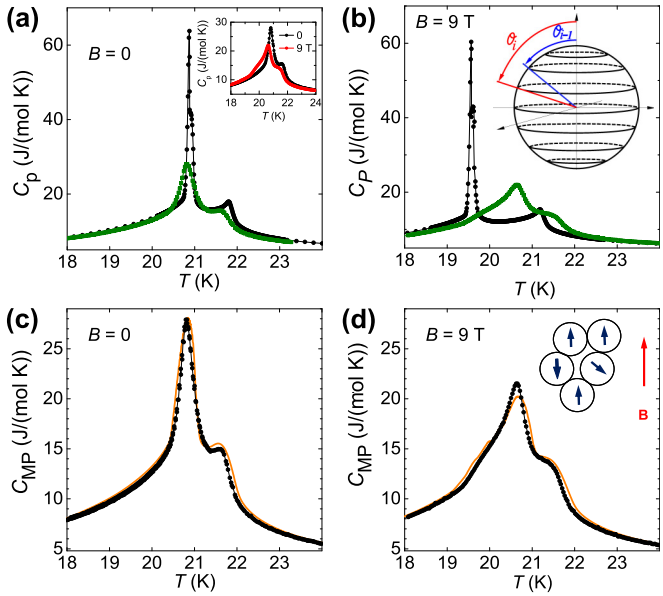

FIG. 9. Specific heat anomalies at the magnetic transitions. (a) and (b) Superimposed total specific heat C_p vs temperature functions measured for the single crystal (full black circles) and for the powder (full green squares) for $B = 0$ and 9 T. (c) and (d) Anomalies of the nonphonon contribution to the powder specific heat $C_{MP}(T)$, measured (full black circles) and calculated (solid orange lines) for $B = 0$ and 9 T. Insets to panels: (a) superimposed anomalies measured for the powder in $B = 0$ and 9 T, (b) polar plot of the uniform distribution of orientations of the c axis in powder grains with respect to **B**, and (d) schematic distribution of orientations of the c axis in powder grains with respect to **B**.

given by the log-normal distribution function:

$$g(t_N, T_N, \sigma) = \frac{1}{\sqrt{2\pi}\sigma t_N}\exp\left[\frac{-(\ln(t_N/T_N))^2}{2\sigma^2}\right], \qquad (16)$$

where σ is the standard deviation, and that it will be sufficient to consider only the t_N values lying within a certain finite range around the arbitrary chosen reference value, $T_R = 20.9$ K. We distinguished $L_l + L_p$ ranges of the width v, where L_l (L_p) denoted the number of ranges with the infimum lower (higher) than T_R. The limits of each of the L_l ranges (a_i, b_i) and its IC-C transition temperature, t_i, were defined as

$$a_i = T_R - v\left(i - \tfrac{1}{2}\right), \quad b_i = T_R - v\left(i - \tfrac{3}{2}\right),$$
$$t_i = T_R - v(i-1), \quad i = 1, 2, \ldots, L_l, \qquad (17)$$

whereas the limits of each of the L_p ranges (c_k, d_k) and its IC-C transition temperature, t_k, were defined as

$$c_k = T_R + v\left(k - \tfrac{1}{2}\right), \quad d_k = T_R + v\left(k + \tfrac{1}{2}\right),$$
$$t_k = T_R + vk, \quad k = 1, 2, \ldots, L_p. \qquad (18)$$

Statistical weight factors with which particular ranges with different t_i (t_k) values entered the total specific heat were estimated by using the expressions:

$$u_{t_i} = \frac{\int_{a_i}^{b_i} g(t, T_N, \sigma)dt}{\int_{a_{L_l}}^{d_{L_p}} g(t, T_N, \sigma)dt} \quad u_{t_k} = \frac{\int_{c_k}^{d_k} g(t, T_N, \sigma)dt}{\int_{a_{L_l}}^{d_{L_p}} g(t, T_N, \sigma)dt}. \qquad (19)$$

Finally, the theoretical nonphonon contribution to the specific heat of the powder sample, C_{MP}, in $B = 0$ was calculated by using the equation

$$C_{MP}(T) = \beta\left(\sum_{i=1}^{L_l} u_{t_i} C_M^{t_i}(T) + \sum_{k=1}^{L_p} u_{t_k} C_M^{t_k}(T)\right), \qquad (20)$$

in which β, σ, L_l, L_p, and v were the fitted parameters. The optimal result, plotted in Fig. 9(c) with the solid orange line, was obtained for $\beta = 0.98$, $\sigma = 0.01$ K, $L_l = 20$, $L_p = 7$, and $v = 0.02$ K. In order to describe the change of position and shape of the anomaly for $B = 9$ T, we took into account that the powder grains closed in the aluminum crucible could not move under influence of B, thus, the distribution of orientation of the c axis of particular grains with respect to the direction of the applied field B, determined by the polar angle θ and the azimuthal angle ϕ, was uniform, as it was illustrated in the inset to Fig. 9(d). The polar plot of this distribution, presented in the inset to Fig. 9(b), has the shape of sphere. The existence of this distribution influences the evolution of the shape of the specific heat anomaly substantially, because, as it was demonstrated in the section "Specific heat of $LiNiPO_4$ single crystal", only the parallel to the c axis component of **B** shifts the magnetic transitions temperatures. Since we measured the single crystal in **B**||**c** for $B = 0, 1, \ldots, 9$ T, we divided the $0^\circ \leqslant \theta \leqslant 90^\circ$ range into 10 intervals, (θ_i, θ_{i+1}) with $i = 0, 1, \ldots, 9$, for which the different parallel to the c axis components of the magnetic field, B_{ci}, were assigned. The limits of these intervals and the B_{ci} values assigned to each interval were defined as

$$\theta_0 = 0, \quad \theta_{10} = \frac{\pi}{2},$$
$$\theta_i = \arccos\left(\frac{9 - i + 1/2}{9}\right) \quad \text{for } i = 1, 2, \ldots, 9,$$
$$B_{ci} = 9 - i \quad \text{for } i = 0, 1, 2, \ldots, 9. \qquad (21)$$

Then, the powder sample mass fractions for which $B_{ci} = (9 - i)$ T, were calculated according to the formula

$$\nu_{9-i} = \frac{1}{2\pi}\int_0^{2\pi}\int_{\theta_i}^{\theta_{i+1}} \sin\theta d\theta d\phi = \cos\theta_i - \cos\theta_{i+1}. \qquad (22)$$

They were found to be equal: $\nu_9 = 1/18$, $\nu_8 = \nu_7 = \cdots = \nu_1 = 1/9$, $\nu_0 = 1/18$. Above, the $\theta \leqslant \pi/2$ values were considered only. However, it has no impact on the result, because the influence of B on the phase transition temperature for θ is exactly the same as for $\pi - \theta$, thus, taking into account the $\theta > \pi/2$ values consists in multiplying the numerator in (22) by 2 and replacing the normalization factor 2π in denominator with 4π. Finally, specific heat C_{I9} of the "ideal," i.e., of nonsmeared T_N, powder placed in $B = 9$ T should be equal to

$$C_{I9}(T) = \sum_{k=0}^{9} \nu_k C_M(T, B = k), \qquad (23)$$

where $C_M(T, B)$ is the specific heat of the single crystal measured in B parallel to the c axis. Next, assuming that B does not affect the smearing of the t_N values considered for the $B = 0$ case, i.e., the values of β, σ, L_l, L_p, u_{t_i}, u_{t_k} and v,

we calculated the specific heat of the real powder in $B = 9$ T by using the following equation:

$$C^{9}_{MP}(T) = \beta\left(\sum_{i=1}^{L_l} u_{t_i} C^{t_i}_{I9}(T) + \sum_{k=1}^{L_p} u_{t_k} C^{t_k}_{I9}(T)\right), \qquad (24)$$

where, like for $B = 0$, $C^{t_i}_{I9}(T) = C_{I9}(T - (t_i - T_N))$. Taking into account simplicity of the proposed model, the calculated dependence, plotted in Fig. 9(d) with the solid orange line, reproduces the experimental dependence quite satisfactorily and proves the validity of our assumptions.

In conclusion, the performed investigation showed that in the $LiNiPO_4$ powder prepared by the standard ceramic high-temperature method, a certain distribution of magnetic properties, resulting in smearing the specific heat anomalies accompanying the magnetic phase transitions, appears. Moreover, the fact, revealed by the single crystal studies, that only **B** directed along the *c* axis influences the temperatures of the magnetic transitions, results in a change of the shape and the temperatures of appearance of the anomalies related to the phase transitions in the powder under influence of the magnetic field.

VI. CONCLUSIONS

$LiNiPO_4$ is a unique representative of the olivines (showing intriguing set of physical properties), because the antiferromagnetic order develops in it in two steps, i.e., on cooling, the second-order transition to the incommensurate phase and then the first-order transition to the commensurate antiferromagnetic phase appear. The present studies were aimed at (i) establishing whether any signatures of existence of a phase transition to the ferroelectric phase and thus, to the multiferroic state, can be found for $LiNiPO_4$, (ii) constructing the detailed $LiNiPO_4$ phase diagram for $B \leqslant 9$ T, (iii) explaining whether the complex exchange interactions and the layered crystalline structure of $LiNiPO_4$ result in any uncommon macroscopic magnetic properties of this compound, and (iv) investigating differences in thermal properties of the powder (the most perspective for application) and the single crystalline samples of $LiNiPO_4$.

In the result of the precise specific heat studies of the $LiNiPO_4$ single crystal, which were "one of the first" successful applications of the "slope analysis procedure," the sharp anomaly accompanying the first-order phase transition from the incommensurate to the commensurate antiferromagnetic phase was shown to be a superposition of two slightly split anomalies. This effect was interpreted as the existence of the two coupled first-order transitions, one of which is evidently the magnetic transition, whereas the nature of the other one is unknown, however possibly, it could be the ferroelectric transition. Thus a certain suggestion that the state below T_N is a multiferroic state has been found. The presence of any observation of a nonzero spontaneous polarization would be a strong argument in favor of our interpretation of the splitting of specific heat anomaly. However, to the best of our knowledge, no observation of the spontaneous polarization in $LiNiPO_4$ was reported till now, despite of the presence of a strong magnetoelectric effect in this compound, which was studied several times (e.g., in Ref. [18]). Nevertheless, for $LiNiPO_4$ the situation is not so clear. For example, the neutron diffraction studies can be described perfectly under assumption that at zero magnetic field, the low-temperature magnetic phase is the purely antiferromagnetic one [9]. However, as it was proved in Ref. [23], a tiny nonzero magnetization, breaking the symmetry in the way "appropriate" for appearance of a tiny nonzero polarization is present, which means that a certain canting of antiferromagnetic sublattices really exists.

Additionally, the specific heat studies allowed to determine the analytic forms of the IC-C and C-P transition lines on the *B*-*T* plane for the magnetic field directed along the *c* axis. The temperatures of both phase transitions were found to decrease parabolically with increase of *B*, i.e., to show the dependence characteristic of two-dimensional antiferromagnetic Ising systems. Moreover, the lattice contribution to the $LiNiPO_4$ specific heat was described analytically by combining the Debye and the Einstein models.

By performing at the same temperatures, the precise, scarcely reported, measurements of magnetization and of magnetic torque as a function of orientation of magnetic field within the same crystalline plane (*a*-*c* and *b*-*c*) and by comparing the obtained functions, we found that the complex exchange interactions, large uniaxial anisotropy and the layered crystalline structure of $LiNiPO_4$ lead to the appearance of the effect that we called "off-diagonal nonlinear magnetic susceptibility," which, to the best of our knowledge, was not reported in the literature. It consists in the fact that the magnetic susceptibility along each od the main crystallographic axes of the orthorhombic $LiNiPO_4$ crystal has a component proportional to the square of the perpendicular to this axis component of the applied magnetic field. The phenomenological model of this effect, describing the experimental data satisfactorily, was proposed.

The specific heat studies of the $LiNiPO_4$ powder (the most attractive for potential applications in the Li-ion batteries) showed that in the powder prepared by the standard ceramic high-temperature method, a certain distribution of properties (induced by structural imperfections and nonstoichiometry), leading to smearing the specific heat anomalies related to the magnetic phase transitions, appears. Moreover, the fact that only **B** directed along the *c* axis influences the temperatures of the magnetic transitions, results in a change of the shape of these anomalies under influence of the magnetic field.

ACKNOWLEDGMENTS

This work was partly supported by the Polish Ministry of Science and Higher Education from funds for science for 2008-2011 years, as a research project (2047/B/H03/2008/34), and by the European Union, within the European Regional Development Fund, through the Innovative Economy grants (POIG.01.01.02-00-108/09 and POIG.01.03.01-00-058/08).

[1] A. K. Padhi, K. S. Nanjundaswamy, and J. B. Goodenough, Phospho-olivines as positive-electrode materials for rechargeable lithium batteries, J. Electrochem. Soc. **144**, 1188 (1997).

[2] S.-Y. Chung, J. T. Bloking, and Y.-M. Chiang, Electronically conductive phospho-olivines as lithium storage electrodes, Nat. Mater. **1**, 123 (2002).

[3] J. Molenda, Lithium-ion batteries - state of art.Novel phospho-olivine cathode materials, Mater. Sci.-Pol. **24**, 61 (2006).

[4] D.-W. Han, Y.-M. Kang, R.-Z. Yin, M.-S. Song, and H.-S. Kwon, Effects of Fe doping on the electrochemical performance of $LiNiPO_4$/C composites for high power-density cathode materials, Electrochem. Commun. **11**, 137 (2009).

[5] A. Kulka, A. Braun, T.-W. Huang, A. Wolska, M. T. Klepka, A. Szewczyk, D. Baster, W. Zając, K. Świerczek, and J. Molenda, Evidence for Al doping in lithium sublattice of $LiFePO_4$, Solid State Ionics **270**, 33 (2015).

[6] D. D. Lecce, R. Verrelli, and J. Hassoun, New lithium ion batteries exploiting conversion/alloying anode and $LiFe_{0.25}Mn_{0.5}Co_{0.25}PO_4$ olivine cathode, Electrochim. Acta **220**, 384 (2016).

[7] L. Qin, Y. Xia, H. Cao, L. Yang, and Z. Liu, Synthesis and electrochemical performance of $LiMn_xFe_y(V)_{1-x-y}PO_4$ cathode materials for lithium-ion batteries, Electrochim. Acta **222**, 1660 (2016).

[8] D. D. Lecce, L. Carbone, V. Gancitano, and J. Hassoun, Rechargeable lithium battery using non-flammable electrolyte based on tetraethylene glycol dimethyl ether and olivine cathodes, J. Power Sources **334**, 146 (2016).

[9] T. B. S. Jensen, N. B. Christensen, M. Kenzelmann, H. M. Rønnow, C. Niedermayer, N. H. Andersen, K. Lefmann, J. Schefer, M. v. Zimmermann, J. Li, J. L. Zarestky, and D. Vaknin, Field-induced magnetic phases and electric polarization in $LiNiPO_4$, Phys. Rev. B **79**, 092412 (2009).

[10] T. B. S. Jensen, N. B. Christensen, M. Kenzelmann, H. M. Rønnow, C. Niedermayer, N. H. Andersen, K. Lefmann, M. Jiménez-Ruiz, F. Demmel, J. Li, J. L. Zarestky, and D. Vaknin, Anomalous spin waves and the commensurate-incommensurate magnetic phase transition in $LiNiPO_4$, Phys. Rev. B **79**, 092413 (2009).

[11] D. Vaknin, J. L. Zarestky, L. L. Miller, J.-P. Rivera, and H. Schmid, Weakly coupled antiferromagnetic planes in single-crystal $LiCoPO_4$, Phys. Rev. B **65**, 224414 (2002).

[12] J. M. Mays, Nuclear magnetic resonances and Mn-O-P-O-Mn superexchange linkages in paramagnetic and antiferromagnetic $LiMnPO_4$, Phys. Rev. **131**, 38 (1963).

[13] N. F. Kharchenko, Y. N. Kharchenko, R. Szymczak, M. Baran, and H. Schmid, Weak ferromagnetism in the antiferromagnetic magnetoelectric crystal $LiCoPO_4$, Low Temp. Phys. **27**, 895 (2001).

[14] N. F. Kharchenko, V. A. Desnenko, Y. N. Kharchenko, R. Szymczak, and M. Baran, Nonmonotonic temperature dependence of the spontaneous magnetization of the antiferromagnetic crystal $LiCoPO_4$, Low Temp. Phys. **28**, 646 (2002).

[15] A. Szewczyk, M. U. Gutowska, J. Wieckowski, A. Wisniewski, R. Puzniak, R. Diduszko, Y. Kharchenko, M. F. Kharchenko, and H. Schmid, Phase transitions in single-crystalline magnetoelectric $LiCoPO_4$, Phys. Rev. B **84**, 104419 (2011).

[16] B. B. Van Aken, J.-P. Rivera, H. Schmid, and M. Fiebig, Observation of ferrotoroidic domains, Nature (London) **449**, 702 (2007).

[17] H. Schmid, Some symmetry aspects of ferroics and single phase multiferroics, J. Phys.: Condens. Matter **20**, 434201 (2008).

[18] D. Vaknin, J. L. Zarestky, J.-P. Rivera, and H. Schmid, Commensurate-Incommensurate Magnetic Phase Transition in Magnetoelectric Single Crystal $LiNiPO_4$, Phys. Rev. Lett. **92**, 207201 (2004).

[19] R. Toft-Petersen, E. Fogh, T. Kihara, J. Jensen, K. Fritsch, J. Lee, G. E. Granroth, M. B. Stone, D. Vaknin, H. Nojiri, and N. B. Christensen, Field-induced reentrant magnetoelectric phase in $LiNiPO_4$, Phys. Rev. B **95**, 064421 (2017).

[20] R. Toft-Petersen, J. Jensen, T. B. S. Jensen, N. H. Andersen, N. B. Christensen, C. Niedermayer, M. Kenzelmann, M. Skoulatos, M. D. Le, K. Lefmann, S. R. Hansen, J. Li, J. L. Zarestky, and D. Vaknin, High-field magnetic phase transitions and spin excitations in magnetoelectric $LiNiPO_4$, Phys. Rev. B **84**, 054408 (2011).

[21] J. Li, T. B. S. Jensen, N. H. Andersen, J. L. Zarestky, R. W. McCallum, J.-H. Chung, J. W. Lynn, and D. Vaknin, Tweaking the spin-wave dispersion and suppressing the incommensurate phase in $LiNiPO_4$ by iron substitution, Phys. Rev. B **79**, 174435 (2009).

[22] V. M. Khrustalyov, V. M. Savytsky, and M. F. Kharchenko, Magnetoelectric effect in antiferromagnetic $LiNiPO_4$ in pulsed magnetic fields, Low Temp. Phys. **42**, 1126 (2016).

[23] Y. N. Kharchenko, N. F. Kharcheno, M. Baran, and R. Szymczak, Weak ferromagnetism and an intermediate incommensurate antiferromagnetic phase in $LiNiPO_4$, Low Temp. Phys. **29**, 579 (2003).

[24] Y. M. Kharchenko, O. V. Miloslavskaya, and M. F. Kharchenko, Linear magneto-optical effect in the incommensurate phase of antiferromagnetic $LiNiPO_4$, Low Temp. Phys. **40**, 1029 (2014).

[25] V. I. Fomin, V. P. Gnezdilov, V. S. Kurnosov, A. V. Peschanskii, A. V. Yeremenko, H. Schmid, J.-P. Rivera, and S. Gentil, Raman scattering in a $LiNiPO_4$ single crystal, Low Temp. Phys. **28**, 203 (2002).

[26] J. Molenda, A. Kulka, A. Milewska, W. Zając, and K. Świerczek, Structural, transport and electrochemical properties of $LiFePO_4$ substituted in lithium and iron sublattices (Al, Zr, W, Mn, Co and Ni), Materials **6**, 1656 (2013).

[27] C. A. Martin, Simple treatment of anharmonic effects on the specific heat, J. Phys.: Condens. Matter **3**, 5967 (1991).

[28] A. Szewczyk, M. Gutowska, B. Dabrowski, T. Plackowski, N. P. Danilova, and Y. P. Gaidukov, Specific heat anomalies in $La_{1-x}Sr_xMnO_3 (0.12 \leqslant x \leqslant 0.2)$, Phys. Rev. B **71**, 224432 (2005).

[29] Physical Property Measurement System, Heat Capacity Option User's Manual, Part No. 1085-150, M5, Quantum Design 2014.

[30] J. Wieckowski, M. U. Gutowska, A. Szewczyk, S. Lewinska, K. Conder, E. Pomjakushina, V. P. Gnezdilov, and S. L. Gnatchenko, Thermal properties of layered cobaltites $RBaCo_2O_{5.5}$ (R = Y, Gd, and Tb), Phys. Rev. B **86**, 054404 (2012).

[31] G. J. Shu, M. W. Wu, and F. C. Chou, Finite-size effect of antiferromagnetic transition and electronic structure in $LiFePO_4$, Phys. Rev. B **86**, 161106(R) (2012).